

# Modeling and Analysis of Nonlinear Axial Force Generated by Automotive Drive-shaft Systems Based on Fractal Theory

Huayuan Feng

South China University of Technology

Wen-Bin Shangguan (✉ [sgwb@scut.edu.cn](mailto:sgwb@scut.edu.cn))

South China University of Technology <https://orcid.org/0000-0003-2454-5593>

---

## Research Article

**Keywords:** Drive-shaft system, Nonlinear generated axial force, Fractal model, Sobol' global sensitivity  
Drive-shaft system, Nonlinear generated axial force, Fractal model, Sobol' global sensitivity

**Posted Date:** March 8th, 2021

**DOI:** <https://doi.org/10.21203/rs.3.rs-284002/v1>

**License:**  This work is licensed under a Creative Commons Attribution 4.0 International License.

[Read Full License](#)

---

# **Modeling and analysis of nonlinear axial force generated by automotive drive-shaft systems based on fractal theory**

Huayuan Feng, Wen-Bin Shangguan\*

(School of Mechanical and Automotive Engineering, South China University of Technology, Guangzhou 510641, China)

\*corresponding author: [sgwb@scut.edu.cn](mailto:sgwb@scut.edu.cn)

**Abstract:** The nonlinear generated axial force (NGAF) of an automotive drive-shaft system is mainly induced by the tripod joint in the drive-shaft system, which will lead to vibration and noise of a vehicle. On the basis of fractal theory, this paper conducts modeling and analysis of the NGAF from the micro level to study the NGAF more effectively. In order to describe the micro contact and friction states between rollers and tracks inside the tripod joint more accurately, a correction method for correcting the distribution function of asperities between rollers and tracks is proposed. Based on the proposed correction method and a calculation model of the NGAF, a fractal model of the NGAF considering rough surface characteristics is established. The fractal model is mainly related to the fractal parameters, the material parameters, the operating conditions and the correction coefficient of the distribution function of asperities. Using Sobol' global sensitivity analysis method, the first order and overall global sensitivities of the fractal model of the NGAF are subsequently analyzed to determine the influence of the factors on the NGAF. The effectiveness of the fractal model and the analytical method for the NGAF is verified by the experiment and calculation examples. The results show that modeling and analysis of the NGAF considering rough surface characteristics are essential to reveal the relationships between the NGAF and the fractal parameters, the material parameters and the correction coefficient from the micro level, which is helpful for the design and analysis of the NGAF of the drive-shaft system.

**Keywords:** Drive-shaft system; Nonlinear generated axial force; Fractal model; Sobol' global sensitivity

## **1. Introduction**

As an important part of automotive transmission systems, the drive-shaft system can transfer the torque from the transmission to the wheel, and ensure the constant speed of the input and output ends at an articulation angle. In general, due to the friction and motion characteristics inside the tripod joint of drive-shaft systems, a periodic axial force, namely, the nonlinear generated axial force (NGAF), will be generated in the operation of drive-shaft systems [1-3]. During the driving process of a vehicle, the NGAF will cause vibration and noise [2-6], thus affecting the comfort of the vehicle. In order to reduce the NGAF of drive-shaft systems, many researchers have studied the NGAF of drive-shaft systems, as well the researches on the NGAF mainly focus on the experimental researches [1-4] and the modeling analyses [5-8].

Since the NGAF is mainly induced by the friction inside the tripod joint, Lee et al. [1-2] developed a special test bench for testing the friction characteristics between rollers and tracks inside the tripod joint under different operation conditions, as well the friction characteristics were modeled and analyzed. In the study, the relationship between the friction characteristics inside the tripod joint and the NGAF was revealed. However, these friction characteristics cannot reflect the influence of the micro contact and friction characteristics between rollers and tracks inside the tripod joint on the NGAF. In order to study and analyze

the NGAF more accurately, Sa et al. [3-4] established a test bench for measuring the NGAF of drive-shaft systems, and studied the influence of the input torque, the type of the tripod joint, the articulation angle and the grease on the NGAF from a macro perspective.

Serveto et al. [5] established an analytic model and a multi-body dynamics model of the NGAF of drive-shaft systems. The two models were mainly related to the input torque, the radius of the tripod joint, the input torque and the Coulomb friction coefficient. In the study, the Coulomb friction coefficient was obtained through minimization of errors between the computed responses and the measured NGAF. Through the kinematic analysis of the tripod joint, Jo et al. [6] established a calculation model for the NGAF of drive-shaft systems with a tripod joint. In the model, two friction models (a pure sliding friction model and a friction model that considers both sliding and rolling friction) were used to characterize the friction. The friction coefficients in the friction models were identified by the measurement. Lim et al. [7-8] established multi-body dynamic models of drive-shaft systems with a tripod joint to analyze the NGAF and the dynamic force inside the tripod joint. In the multi-body dynamic models, the Coulomb friction model was used to characterize the friction, while the impact function (which is mainly related to the contact stiffness, the force exponent and the penetration displacement of contact pairs) was used to calculate the normal contact force. However, neither the Coulomb friction model nor the impact function could reflect the micro friction and contact characteristics between contact pairs.

In the aforementioned studies, neither the experimental research nor the modeling analysis of the NGAF considered the influence of micro contact and friction characteristics between the contact pairs inside the tripod joint on the NGAF. In addition, the friction coefficient, which has great influence on the NGAF, was generally identified through minimization of errors between the computed responses and the measured data from a macro perspective. The friction coefficient obtained by the measurement identification, however, cannot directly reflect the influence of the micro characteristics of rough surfaces on the NGAF. Analyzing the influence of the micro characteristics of the rough surface on the NGAF allow us to find the root cause of the NGAF, which is beneficial to the design and optimization of the NGAF of the drive-shaft system. Thus, in order to study the NGAF more effectively, it is essential to consider the influence of the rough surface characteristics between rollers and tracks inside the tripod joint on the NGAF.

Since fractal parameters (which are used to characterize rough surface profiles) of fractal theory do not depend on the sampling length and the instrument resolution [9,10], the fractal theory has a good applicability in the study of mechanical rough surfaces, and thus the fractal theory is usually used to analyze the micro characteristics of contact pairs in practical engineering [11-15]. In the fractal theory analysis, the

contact between two rough surfaces is generally regarded as the contact between a flat plane and a rough plane, as well the distribution function of the contact asperities is used to describe the distribution of the contact asperities on the rough plane [16,17]. The contact between rollers and tracks inside the tripod joint, however, is a contact between a spherical surface and a cylindrical surface. Thus, it is necessary to modify the distribution function of the contact asperities so as to obtain the distribution of the contact asperities between rollers and tracks more accurately. In addition, the sensitivity analysis of the NGAF can be performed to obtain the influence of various factors on the NGAF, thus providing guidance for the design and optimization of the NGAF of drive-shaft systems. The primary goals and the contributions of the study are summarized below.

Based on fractal theory and a calculation model of the NGAF, a fractal model of the NGAF considering rough surface characteristics is established. The fractal model of the NGAF is mainly related to the fractal parameters (namely, the fractal dimension and the characteristic length scale), the yield strength, the elastic modulus, the Poisson's ratio, the articulation angle, the shaft angular position of the drive-shaft system and the correction coefficient of the distribution function of contact asperities between rollers and tracks. To describe the contact and friction states between rollers and tracks inside the tripod joint more accurately, a correction method for the distribution function of contact asperities between rollers and tracks is proposed. Using Sobol' global sensitivity analysis method, the first order global sensitivity and the overall global sensitivity of the fractal model of the NGAF are subsequently analyzed to determine the influence of various factors on the NGAF.

The remaining paper is organized in four different sections. In Section 2, a calculation model of the NGAF is introduced. The fractal model of the NGAF of the drive-shaft system is proposed in Section 3 together with the correction method for the distribution function of contact asperities between rollers and tracks. In Section 4, the measurement method for the NGAF of a drive-shaft system is briefly described together with the model verification, as well the analysis of effects of the factors on the NGAF and the sensitivity analysis of the fractal model of the NGAF are performed through numerical examples. The key conclusions of the study are summarized in Section 5.

## 2. A calculation model of the NGAF of the drive-shaft system

### 2.1 Structures of a drive-shaft system and a tripod joint

A drive-shaft system is mainly composed of a ball joint, a tripod joint and a drive-shaft, as shown in Fig. 1(a). The ball joint is connected to the wheel, while the tripod joint is connected to the transmission. In a drive-shaft system, the NGAF is mainly induced by the tripod joint. The structure of a tripod joint is

shown in Fig. 1(b). A tripod joint generally comprises rollers (1), needles (2), a tripod (4) and a housing (6). There are three tracks (5) parallel to the input shaft for the rollers to roll and slide, as well there is a certain amount of grease in the housing. The tripod has three trunnions (4), 120 degrees apart, which are used for assembling needles and rollers.

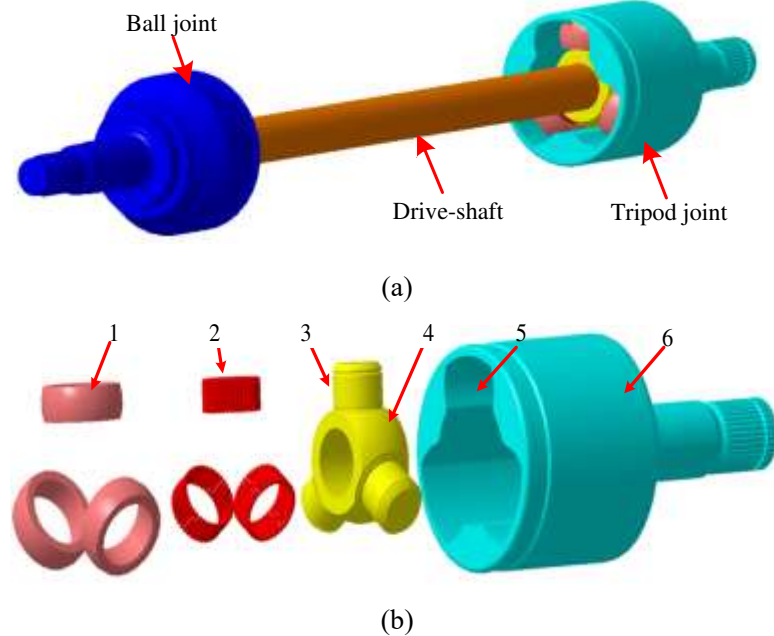


Fig. 1: (a) Structure of a drive-shaft system; and (b) Structure of a tripod joint. (1-roller; 2-needle; 3-trunnion; 4-tripod; 5-track; 6-housing)

## 2.2 Main kinematics results of the drive-shaft system with a tripod joint

The NGAF is related to the kinematics of the drive-shaft system with a tripod joint, and the kinematics have been described in [5,18]. Briefly, the schematic diagram of the kinematic model of a drive-shaft system is shown in Fig. 2, where the ball joint is simplified as a fixed point  $A$ , and the coordinate system  $B-x_1y_1z_1$  is established with the center  $B$  of the inner bottom surface of the housing as the origin. In the coordinate system  $B-x_1y_1z_1$ , the axis  $z_1$  coincides with the center axis of the housing; the axis  $y_1$  is in the vertical direction; and the axis  $x_1$  is perpendicular to both the  $y_1$  and  $z_1$  axes. Under an articulation angle  $\delta$  and an input angle  $\varphi$ , the shaft angular position of the drive-shaft system is  $\theta$ , as well the motion equations of the rollers  $C_i$  ( $i=1,2,3$ ) along the central axis of the housing and along the central axis of the trunnions of the tripod are as follows [5]:

$$l_i = z + r_i \sin \delta \cos \varphi_i, r_i = r + e(1 + 2 \cos 2\varphi_i), i = 1,2,3 \quad (1)$$

where  $r$  is the pitch circle radius (PCR) of the tripod joint;  $e$  is the offset, which is defined as the distance between point  $C$  and axis  $z_1$ ;  $\varphi_i$ ,  $z$  and  $e$  are expressed as [5]:

$$\varphi_i = \varphi + (i - 1) \frac{2\pi}{3}, z = D_d - L \cos \delta, e = \frac{r}{2} \left( \frac{1}{\cos \delta} - 1 \right), i = 1,2,3 \quad (2)$$

where  $D_d$  is the distance between point  $A$  and axis  $z_1$ ;  $L$  is the length of the drive-shaft.

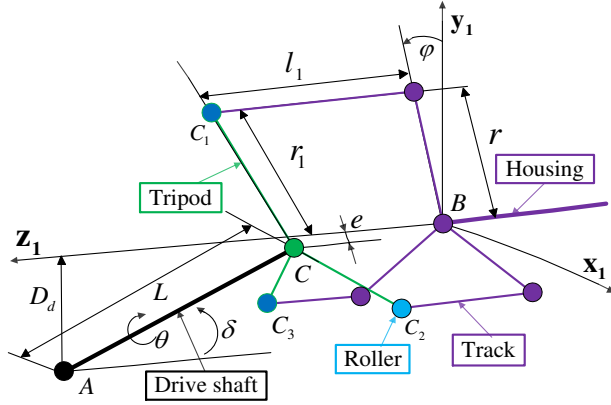


Fig. 2: Schematic diagram of the kinematic model of a drive-shaft system.

Taking roller  $C_1$  in the Fig. 2 as the research object, its movement on the track is shown in Fig. 3. The axis system of the track ( $i_0, j_0$ ) and that of the roller ( $i_1, j_1$ ) correspond to the instantaneous position, and  $C_o$  is the origin of both the axis systems. In addition,  $V_c$  is the velocity of roller  $C_1$  in direction  $j_0$ , as well  $\lambda_1$  is the deflection angle of roller  $C_1$ . During the operation of the drive-shaft system, the roller slides in direction  $i_1$  and rolls in direction  $j_1$ , and thus there are sliding friction and rolling friction between the roller and the track in direction  $i_1$  and direction  $j_0$ , respectively. Since the sliding friction coefficient between the roller and the track is much greater than the rolling friction coefficient [2, 5], only the sliding friction between the roller and the track was considered in this paper.

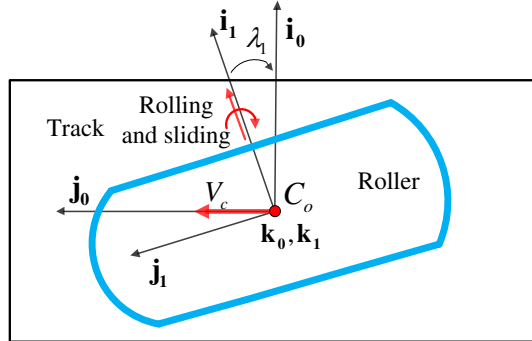


Fig. 3: Schematic diagram of the motion of roller  $C_1$  on the tracks.

According to Fig. 3, the velocity  $V_{i_1}$  of roller  $C_1$  in direction  $i_1$  is obtained as:  $V_{i_1} = V_c \sin \lambda_1 = \dot{l}_1 \sin \lambda_1$ , where  $\dot{l}_1$  can be determined on the basis of the motion equation of roller  $C_1$  along the central axis  $z_1$  shown in Eq. (1). Thus, in an ideal condition, the velocity  $V_{i_1}$  is expressed as:

$$V_{i_1} = \dot{l}_1 \sin \lambda_1 = -r\dot{\theta} \sin \delta \sin \varphi_1 \sin \lambda_1 \quad (3)$$

In addition, the relationship among the deflection angle  $\lambda_1$ , the articulation angle  $\delta$  and the shaft angular position  $\varphi_1$  is obtained as [18]:

$$\sin \lambda_1 = -\delta \cos \varphi_1 \quad (4)$$

### 2.3 A calculation model of the NGAf of the drive-shaft system

The schematic diagram of the normal force of rollers acting on tracks is shown in Fig. 4.  $F_n^i$  ( $i=1,2,3$ )

are the normal forces of rollers  $C_i$  acting on the tracks, as well  $T$  is the input torque. In an ideal condition, the offset  $e$  in Fig. 2 can be ignored, and according to Eq. (1), it is obtained:

$$r_1 \approx r_2 \approx r_3 \approx r \quad (5)$$

Thus, the normal forces  $F_n^i$  ( $i=1,2,3$ ) of rollers  $C_i$  acting on the tracks are:

$$F_n^1 \approx F_n^2 \approx F_n^3 \approx \frac{T}{3r} = F_n \quad (6)$$

where  $F_n$  is the normal force between the roller and the track in the ideal condition.

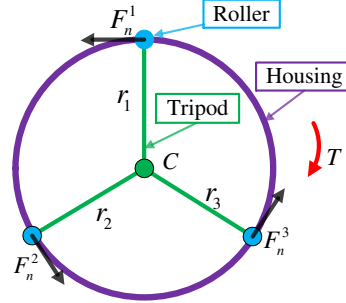


Fig. 4: Schematic diagram of the normal force of rollers acting on tracks.

According to Fig. 3, when roller  $C_1$  slides along direction  $\mathbf{i}_1$ , the sliding friction force is obtained as:

$$F_f^1 = F_n^1 \mu \text{sign}(V_{i_1}) \approx F_n \mu \text{sign}(V_{i_1}) \quad (7)$$

where  $\mu$  is the sliding friction coefficient; and  $\text{sign}(\cdot)$  denotes the sign of the velocity  $V_{i_1}$ .

And then the component of the friction force  $F_f^1$  in the direction  $\mathbf{j}_0$  is:

$$F_1 = F_f^1 \sin \lambda_1 \quad (8)$$

Thus, combining Eqs. (3), (4), (7) and (8), the component of the friction force  $F_f^1$  along the direction  $\mathbf{j}_0$ , namely, the NGAF between roller  $C_1$  and the track, can be expressed as:

$$F_1 = F_n^1 \mu \sin \lambda_1 \text{sign}(V_{i_1}) \approx F_n \mu (-\delta \cos \varphi_1) \text{sign}(r \dot{\theta} \sin \delta \sin \varphi_1 (\delta \cos \varphi_1)) \quad (9)$$

In general, the input angle  $\varphi$  is equal to the shaft angular position  $\theta$ , and according to Eq. (2),  $\varphi_1 = \theta$ . Eq. (9) thus can be obtained as:

$$F_1 = F_n \mu (-\delta \cos \theta) \text{sign}(r \dot{\theta} \sin \delta \sin \theta (\delta \cos \theta)) \quad (10)$$

Similarly, the NGAFs  $F_i$  ( $i=2,3$ ) between rollers  $C_i$  and the tracks can be obtained as follows:

$$F_i = F_n^i \mu (-\delta \cos \varphi_i) \text{sign}(r \dot{\theta} \sin \delta \sin \varphi_i (\delta \cos \varphi_i)) \approx F_n \mu A_i \quad (11)$$

where  $A_i$  is:

$$A_i = -\delta \cos \left( \theta + (i-1) \frac{2\pi}{3} \right) \text{sign} \left( r \dot{\theta} \sin \delta \sin \left( \theta + (i-1) \frac{2\pi}{3} \right) \delta \cos \left( \theta + (i-1) \frac{2\pi}{3} \right) \right), i = 1,2,3 \quad (12)$$

The total NGAF of the drive-shaft system, thus, is obtained:

$$F = F_1 + F_2 + F_3 = \sum_{i=1}^3 F_i \approx \sum_{i=1}^3 F_n \mu A_i \quad (13)$$

It is seen from Eqs. (12) and (13) that the magnitude of the NGAF mainly depends on the friction coefficient  $\mu$ , the normal force  $F_n$ , the articulation angle  $\delta$  and the shaft angular position  $\theta$  of the drive-shaft system. In addition, the NGAF changes periodically with the shaft angular position. When the shaft angular position is  $90^\circ$ , the magnitude of the AFF reaches the maximum [18]. In practical engineering, most attention is paid to the maximum magnitude of the AFF, and thus the shaft angular position is set as  $90^\circ$  in the following analysis.

### 3. A fractal model of the NGAF of the drive-shaft system

In Eq. (13), the normal force and the friction coefficient are macro influencing factors, which cannot directly reflect the influence of the micro contact and friction characteristics between rollers and tracks on the NGAF. In order to study the NGAF more deeply and effectively, fractal models for calculating the normal force and the friction coefficient considering rough surface characteristics are first proposed based on fractal theory, and then the fractal model for calculating the NGAF is proposed by combining Eq. (13) and the fractal models of the normal force and the friction coefficient. In addition, since the contact between rollers and tracks is a contact between a spherical surface and a cylindrical surface, a correction method for the distribution function of contact asperities between rollers and tracks is proposed to describe the contact state between rollers and tracks more accurately.

#### 3.1 Fractal function, and deformation characteristics of asperities

The two-dimensional surface profile of the mechanical rough surface can be characterized by the Weierstrass-Mandelbrot (W-M) fractal function [16, 19]:

$$z(x) = L \left( \frac{G}{L} \right)^{D-1} (\ln \gamma)^{1/2} \sum_{n=n_l}^{\infty} \gamma^{(D-2)/n} \left[ \cos \phi_n - \cos \left( \frac{2\pi \gamma^n x}{L} - \phi_n \right) \right], \quad 1 < D < 2, \gamma > 1 \quad (14)$$

The meanings of symbols in Eq. (14) are shown in Table 1. According to the research in [10, 16],  $\gamma = 1.5$  is a suitable value for high spectral density and phase randomization. In addition,  $D$  and  $G$  are important parameters affecting the roughness and rough surface characteristics of a rough surface.

Table 1: Meanings of symbols in Eq. (14).

Symbol	Meaning	Symbol	Meaning
$z$	Surface height	$L$	Sample length
$x$	Lateral distance	$\phi_n$	Random phase
$D$	Fractal dimension of the rough surface	$\gamma$	Parameter for determining the spectral density and self-affine
$G$	Characteristic length scale of the rough surface	$n_l$	Parameter corresponding to the low cut-off frequency of the surface contour

For a single contact spot on the rough surface, the schematic diagram of its deformation is shown in Fig. 5. In Fig. 5,  $\sigma$  is the deformation displacement of the asperity;  $R$  is the radius of the asperity base;  $r_a$  is the radius of the actual contact area;  $r_n$  is the radius of the nominal contact area. The deformation

displacement  $\sigma$  depends on the values of the peak and trough of the surface profile, and  $\sigma$  can be expressed as follows [16, 19]:

$$\sigma = 2G^{D-1}(\ln\gamma)^{1/2}(2r_n)^{2-D} \quad (15)$$

According to Fig. 5, the radius  $R$  of the asperity can be expressed as:

$$R^2 = (R - \sigma)^2 + r_n^2 \quad (16)$$

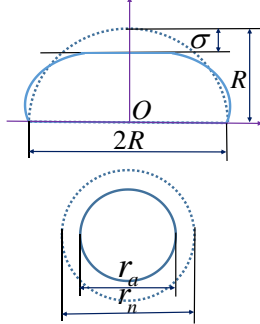


Fig. 5: Schematic diagram of the deformation of a contact spot.

Since  $R$  is much greater than  $\sigma$  during the deformation of the asperity, according to Eq. (16), it is obtained:

$$r_n^2 \approx 2R\sigma \quad (17)$$

The nominal contact area  $a_n$  can be expressed as follows:

$$a_n = \pi r_n^2 \quad (18)$$

Combining Eqs. (15), (17) and (18), it is obtained:

$$R = \frac{r_n^2}{2\sigma} = \frac{a_n^{D/2}}{2^{4-D}\pi^{D/2}G^{D-1}(\ln\gamma)^{1/2}} \quad (19)$$

In general, the deformation of the asperity can be divided into two stages: the elastic deformation stage and the plastic deformation stage. When the contact area of the asperity is greater than the critical contact area, the asperity is in the elastic deformation; when the contact area of the asperity is smaller than the critical contact area, the asperity is in the plastic deformation stage [16]. The critical contact area  $a_n^c$  can be expressed as [16]:

$$a_n^c = \left[ 2^{7-2D}\pi^{D-3} \left( \frac{2E^*}{qKY} \right)^2 G^{2D-2} \ln\gamma \right]^{1/(D-1)} \quad (20)$$

where,  $K$  is the ratio of the hardness  $H$  of the softer material to its yield strength  $Y$ ;  $q$  is related to the Poisson's ratio of the softer material; and  $E^*$  is the equivalent elastic modulus. The value of  $K$  is generally taken as 2.8, as well  $q$  and  $E^*$  can be expressed as [16]:

$$q = 0.454 + 0.41\nu_1, \frac{1}{E^*} = \frac{1 - \nu_1^2}{E_1} + \frac{1 - \nu_2^2}{E_2} \quad (21)$$

where  $E_1$  and  $E_2$  are the elastic moduli of the two contact materials, respectively, as well  $\nu_1$  and  $\nu_2$  are the

Poisson's ratios of the softer and harder contact materials, respectively.

In the elastic deformation stage, according to Hertz theory, the normal contact force  $F_e$  and the contact area  $a_e$  of the asperity can be expressed as [10]:

$$F_e = \frac{4E^*R^{1/2}\sigma^{3/2}}{3}; \quad a_e = \pi R\sigma \quad (22)$$

Substituting Eqs. (15) and (19) into Eq. (22), it is obtained:

$$F_e = \frac{\frac{9}{2^{2-D}}\pi^{(D-3)/2}E^*G^{D-1}(\ln\gamma)^{1/2}}{3}a_n^{(3-D)/2}; \quad a_e = a_n/2 \quad (23)$$

In the plastic deformation stage, the normal contact force  $F_p$  and the contact area  $a_p$  of the asperity can be expressed as [10]:

$$F_p = KYa_n; \quad a_p = a_n \quad (24)$$

### 3.2 Correction method for the distribution function of asperities between the roller and the track

In general, the contact of two rough surfaces can be regarded as the contact between a flat plane and a rough plane. In the contact process, the relationship between the number  $n$  of asperities and the contact area  $a$  of asperities, that is, the distribution function  $n(a)$  of asperities, can be expressed as [20, 21]:

$$\begin{cases} n(a) = \frac{D}{2}\psi^{(2-D)/2}a_l^{D/2}a^{-(D+2)/2} \\ \frac{\psi^{(2-D)/2} - (1 + \psi^{-D/2})^{-(2-D)/D}}{(2-D)/D} = 1 \\ a_l = \frac{2-D}{D}\psi^{(2-D)/2}A_r \end{cases} \quad (25)$$

where,  $a_l$  is the nominal maximum contact area of asperities,  $A_r$  is the actual contact area of the two contact surfaces; and  $\psi$  is the correction factor for the ratio of the actual contact area  $A_r$  to the maximum contact area  $a_l$  of asperities [21].

However, since the outer surface of the roller and the inner surface of the track are a spherical surface and a cylindrical surface, respectively, the contact between the roller and the track can be regarded as a point contact between a spherical surface and a cylindrical surface, as shown in Fig. 6. In the figure,  $O$  and  $F_n$  are the contact point and the normal force between the roller and the track, respectively;  $R_1$  and  $R_2$  are the radius of the track cross section and the radius of the roller, respectively;  $\alpha$  and  $L_t$  are the arc angle of the track cross section and the length of the track, respectively. It is seen from Fig. 6 that the contact between the roller and the track inside the tripod joint is the contact between two curved surfaces, and thus Eq. (25) is not applicable to the contact between the roller and the track. To reflect the distribution of asperities between the roller and the track more accurately, it is necessary to improve Eq. (25).

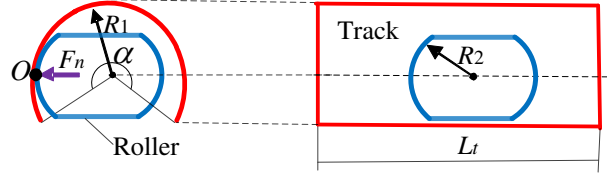


Fig. 6: Schematic diagram of the contact between the roller and the track.

For the contact between two rough curved surfaces, the improved distribution function  $n^*(a)$  of asperities can be expressed as [22, 23]:

$$n^*(a) = \chi n(a) = \chi \frac{D}{2} \psi^{(2-D)/2} a_l^{D/2} a^{-(D+2)/2} \quad (26)$$

where  $\chi$  is the correction coefficient of the improved distribution function  $n^*(a)$  of asperities, and it can be expressed as [22, 23]:

$$\chi = \left( \frac{S_t}{S_w} \right)^{K_h} \quad (27)$$

where,  $S_t$  is the theoretical contact area between two contact surfaces;  $K_h$  is the comprehensive curvature coefficient; and  $S_w$  is the sum of the surface areas of the two contact surfaces:

$$S_w = S_1 \pm S_2 \quad (28)$$

where  $S_1$  and  $S_2$  are the surface areas of the two contact surfaces, respectively. In addition, "+" is for the external contact, while "-" is for the internal contact [23].

### 3.2.1 Comprehensive curvature coefficient between the roller and the track

The schematic diagram of the static contact between two curved surfaces is shown in Fig. 7(a). Suppose two uniform and isotropic surfaces I and II contact at point  $O$ . The coordinate systems  $O-u_1v_1w_1$  are fixed to surface I, while the coordinate systems  $O-u_2v_2w_2$  are fixed to surface II. The positive directions of  $w_1$  and  $w_2$  correspond to the inner normal directions of surfaces I and II, respectively. And  $F_l$  is the load.



Fig. 7: (a) Schematic diagram of the static contact between two curved surfaces; and (b) schematic diagram of the coordinates of the two surfaces at the contact point  $O$ .

Near the contact point  $O$ , the surface equations of surfaces I and II are respectively [22]:

$$w_1 = f_1(u_1, v_1), \quad w_2 = f_2(u_2, v_2) \quad (29)$$

Thus, near the contact point  $O$ , the curvatures of surface I corresponding to directions  $u_1$  and  $v_2$  are

respectively:

$$K_{11} = \frac{\partial^2 f_1}{\partial u_1^2} \Big|_0, \quad K_{12} = \frac{\partial^2 f_2}{\partial v_2^2} \Big|_0 \quad (30)$$

Similarly, near the contact point  $O$ , the curvatures of surface II corresponding to directions  $u_2$  and  $v_1$  are respectively:

$$K_{21} = \frac{\partial^2 f_2}{\partial u_2^2} \Big|_0, \quad K_{22} = \frac{\partial^2 f_1}{\partial v_1^2} \Big|_0 \quad (31)$$

And then the comprehensive curvature coefficient between two curved surfaces is obtained:

$$K_h = K_{11} + K_{12} + K_{21} + K_{22} \quad (32)$$

It is seen from the Fig. 6 that the contact between the roller and the track can be regarded as an internal contact between a spherical surface and a cylindrical surface. According to Eq. (29) and Fig. 6, the equations of the spherical surface and the cylindrical surface near the contact point  $O$  are obtained, respectively:

$$-w_1 = (R_2^2 - u_1^2 - v_1^2)^{1/2}, \quad w_2 = (R_1^2 - v_2^2)^{1/2} \quad (33)$$

Substituting Eqs. (30), (31) and (33) into Eq. (32), the comprehensive curvature coefficient  $K_h$  between the roller and the track can be obtained as follows:

$$K_h = \frac{2}{R_2} - \frac{1}{R_1} \quad (34)$$

### 3.3.2 Correction coefficient for the distribution function of asperities between the roller and the track

According to Hertz theory, for the point contact, the theoretical contact area  $S_t$  between two contact surfaces is [6, 24]:

$$\begin{aligned} S_t &= \pi \sqrt[3]{(3F_n/4E^*)^2 (R_{eq1} R_{eq2})} \\ R_{eq1} &= \left( \frac{1}{R_1} + \frac{1}{R_3} \right)^{-1}; \quad R_{eq2} = \left( \frac{1}{R_2} + \frac{1}{R_4} \right)^{-1} \end{aligned} \quad (35)$$

where,  $R_{eq1}$  and  $R_{eq2}$  are the equivalent radii;  $R_1$  and  $R_3$  are the radii of surface I;  $R_2$  and  $R_4$  are the radii of surface II. For the contact between the track and the roller,  $R_3$  and  $R_4$  are respectively [6]:

$$R_3 = \infty; \quad R_4 = R_2 \quad (36)$$

Combining Eqs. (35) and (36), the theoretical contact area between the track and the roller is obtained:

$$S_t = \pi \sqrt[3]{(3F_n/4E^*)^2 (R_1 R_2 / 2)} \quad (37)$$

According to Eq. (28) and Fig. 6, the sum of the surface areas of the spherical surface and the cylindrical surface is:

$$S_w = S_2 - S_1 = \alpha R_1 L_t - 4\pi R_2^2 \quad (38)$$

where the outer surface of the roller is regarded as a complete spherical surface.

In addition, since the materials of the roller and the track are basically the same, the elastic modulus

and Poisson's ratio of the roller are generally regarded as equal to the elastic modulus and Poisson's ratio of the track in the analysis [25]:

$$\nu_1 = \nu_2; E_1 = E_2 \quad (39)$$

According to Eqs. (21) and (39), the equivalent elastic modulus can be expressed as:

$$E^* = \frac{E_1}{2(1 - \nu_1^2)} \quad (40)$$

Substituting Eqs. (6), (34), (37), (38) and (40) into Eq. (27), the correction coefficient  $\chi$  of the distribution function of asperities between the roller and the track can be obtained, as follows:

$$\chi = \left( \frac{\pi \sqrt[3]{\left(3F_n/(4E^*)\right)^2 (R_1 R_2 / 2)}}{\alpha R_1 L_t - 4\pi R_2^2} \right)^{\left(\frac{2}{R_2} - \frac{1}{R_1}\right)} = \left( \frac{\pi \sqrt[3]{\left(\frac{T(1 - \nu_1^2)}{2rE_1}\right)^2 (R_1 R_2 / 2)}}{\alpha R_1 L_t - 4\pi R_2^2} \right)^{\left(\frac{2}{R_2} - \frac{1}{R_1}\right)} \quad (41)$$

### 3.3 Fractal model of the normal contact force between the roller and the track

According to Eq. (13), the normal force  $F_n$  of the roller acting on the track is an important factor affecting the NGAF. Under the action of the normal force  $F_n$ , there is a normal contact force between the roller and the track, which is equal to but opposite to the normal force  $F_n$ . In the elastic deformation stage, according to Eqs. (23), (26), (40) and (41), the fractal model of the normal contact force between the roller and the track can be obtained as follows:

$$F_{N_e} = \int_{a_n^c}^{a_l} n^*(a_n) F_e da_n = \begin{cases} \frac{2^{(7-3D)/2} \chi D G^{D-1} E_1 (\ln \gamma)^{1/2} \psi^{(2-D)/2}}{3\pi^{(3-D)/2} (3-2D) (1-\nu_1^2) a_l^{-D/2}} \left( a_l^{\frac{(3-2D)}{2}} - (a_n^c)^{\frac{(3-2D)}{2}} \right), & \text{for } D \neq 1.5 \\ \frac{\pi^{-4/3} \chi G^{1/2} E_1 (\ln \gamma)^{1/2} \psi^{1/4} a_l^{3/4} \ln(a_l/a_n^c)}{(1-\nu_1^2)}, & \text{for } D = 1.5 \end{cases} \quad (42)$$

In the plastic deformation stage, according to Eqs. (24), (26) and (41), the fractal model of the normal contact force between the roller and the track can be obtained as follows:

$$F_{N_p} = \int_0^{a_n^c} n^*(a_n) F_p da_n = \begin{cases} \frac{\chi K Y D \psi^{(2-D)/2}}{2-D} a_l^{D/2} (a_n^c)^{\frac{(2-D)}{2}}, & \text{for } D \neq 1.5 \\ 3\chi K Y \psi^{1/4} a_l^{3/4} (a_n^c)^{1/4}, & \text{for } D = 1.5 \end{cases} \quad (43)$$

where  $a_l$  and  $a_n^c$  are the nominal maximum contact area and nominal critical contact area of asperities, respectively. The relationship between the nominal maximum contact area  $a_l$  and the actual maximum contact area  $a_{real}$  of asperities, and the relationship between the nominal critical contact area  $a_n^c$  and the actual critical contact area  $a_{real}^c$  are as follows [16, 26]:

$$a_{real} = \frac{a_l}{2}; a_{real}^c = \frac{a_n^c}{2} \quad (44)$$

Combining Eqs. (42), (43) and (44), the fractal model of the total normal contact force between the roller and the track is obtained:

$$F_{N_t} = F_{N_e} + F_{N_p} = \chi \begin{cases} \frac{2^{\frac{(10-3D)}{2}} D G^{D-1} E_1(\ln\gamma)^{\frac{1}{2}} \psi^{\frac{(2-D)}{2}}}{3\pi^{\frac{(3-D)}{2}} (3-2D)(1-\nu_1^2) a_{real}^{-\frac{D}{2}}} \left( a_{real}^{\frac{(3-2D)}{2}} - (a_{real}^c)^{\frac{(3-2D)}{2}} \right) + \\ \frac{2KYD\psi^{(2-D)/2}}{2-D} a_{real}^{D/2} (a_{real}^c)^{\frac{(2-D)}{2}} \\ \left[ \frac{\frac{3}{2}\pi^{-\frac{4}{3}}G^{\frac{1}{2}}E_1(\ln\gamma)^{\frac{1}{2}}\psi^{\frac{1}{4}}a_{real}^{\frac{3}{4}}\ln\left(\frac{a_{real}}{a_{real}^c}\right)}{(1-\nu_1^2)} + \right], \text{for } D \neq 1.5 \\ \frac{6KY\psi^{1/4}a_{real}^{3/4}(a_{real}^c)^{1/4}}{6-3\nu_1} \end{cases}, \text{for } D = 1.5 \quad (45)$$

### 3.4 Fractal model of the friction coefficient between the roller and the track

The friction coefficient  $\mu$  in Eq. (13) is another important factor affecting the NGAF, which is related to the normal and tangential contact forces between the roller and the track. When a single asperity yields, the tangential contact force of the asperity can be expressed as [26]:

$$F_t = \frac{8r_n^2}{6-3\nu_1} Y + \frac{8(2\nu_1-1)}{(6-3\nu_1)\pi} F_e = \frac{4a_n}{(6-3\nu_1)\pi} Y + \frac{8(2\nu_1-1)}{(6-3\nu_1)\pi} F_e \quad (46)$$

According to Eqs. (23), (26), (44) and (46), the tangential contact force between the roller and the track can be obtained:

$$F_{T_f} = \int_{a_n^c}^{a_l} n^*(a_n) F_t da_n =$$

$$\begin{cases} \frac{8\chi D \psi^{\frac{(2-D)}{2}} Y}{(2-D)(6-3\nu_1)\pi} \left( a_{real} - a_{real}^{\frac{D}{2}} (a_{real}^c)^{\frac{(3-2D)}{2}} \right) + \\ \left[ \frac{2^{\frac{(17-3D)}{2}} \chi D E_1 G^{D-1} (\ln\gamma)^{\frac{1}{2}} \psi^{\frac{(2-D)}{2}} (2\nu_1-1)}{3\pi^{(5-D)/2} (3-2D)(6-3\nu_1)(1-\nu_1^2)} a_{real}^{\frac{D}{2}} \left( a_{real}^{\frac{(3-2D)}{2}} - (a_{real}^c)^{\frac{(3-2D)}{2}} \right) \right], \text{for } D \neq 1.5 \\ \left[ \frac{8\chi \psi^{\frac{1}{4}} Y}{(2-\nu_1)\pi} \left( a_{real} - a_{real}^{\frac{3}{4}} (a_{real}^c)^{\frac{1}{4}} \right) + \frac{2^{\frac{15}{4}} \chi G^{\frac{1}{2}} E_1 (\ln\gamma)^{\frac{1}{2}} \psi^{\frac{1}{4}} (2\nu_1-1)}{\pi^{\frac{7}{4}} (1-\nu_1^2) (6-3\nu_1)} a_{real}^{\frac{3}{4}} \ln\left(\frac{a_{real}}{a_{real}^c}\right) \right], \text{for } D = 1.5 \end{cases} \quad (47)$$

According to Eqs. (45) and (47), the fractal model of the friction coefficient between the roller and the track, thus, can be expressed as:

$$\mu = \frac{F_{T_f}}{F_{N_t}} \quad (48)$$

### 3.5 A fractal model of the NGAF of the drive-shaft system

Combining Eqs. (13), (45), (47) and (48), the fractal model of the NGAF of the drive-shaft system can be obtained as follows:

$$F = \sum_{i=1}^3 F_n \mu A_i = \sum_{i=1}^3 F_{N_t} \left( \frac{F_{T_f}}{F_{N_t}} \right) A_i = \sum_{i=1}^3 A_i \cdot \quad (49)$$

$$\left[ \frac{8\chi D \psi^{\frac{(2-D)}{2}} Y}{(2-D)(6-3\nu_1)\pi} \left( a_{real} - a_{real}^{\frac{D}{2}} (a_{real}^c)^{\frac{(3-2D)}{2}} \right) + \frac{2^{\frac{(17-3D)}{2}} \chi D E_1 G^{D-1} (\ln \gamma)^{\frac{1}{2}} \psi^{\frac{(2-D)}{2}} (2\nu_1 - 1)}{3\pi^{(5-D)/2} (3-2D)(6-3\nu_1)(1-\nu_1^2)} a_{real}^{\frac{D}{2}} \left( a_{real}^{\frac{(3-2D)}{2}} - (a_{real}^c)^{\frac{(3-2D)}{2}} \right) \right], \text{for } D \neq 1.5$$

$$F = \sum_{i=1}^3 F_n \mu A_i = \sum_{i=1}^3 F_{N_t} \left( \frac{F_{T_f}}{F_{N_t}} \right) A_i = \sum_{i=1}^3 A_i .$$

$$\left[ \frac{8\chi \psi^{\frac{1}{4}} Y}{(2-\nu_1)\pi} \left( a_{real} - a_{real}^{\frac{3}{4}} (a_{real}^c)^{\frac{1}{4}} \right) + \frac{2^{\frac{15}{4}} \chi G^{\frac{1}{2}} E_1 (\ln \gamma)^{\frac{1}{2}} \psi^{\frac{1}{4}} (2\nu_1 - 1)}{\pi^{\frac{7}{4}} (1-\nu_1^2) (6-3\nu_1)} a_{real}^{\frac{3}{4}} \ln \left( \frac{a_{real}}{a_{real}^c} \right) \right], \text{for } D = 1.5$$

where,  $A_i$  is expressed as Eq. (12).

From Eq. (49), it is seen that the NGAF of the drive-shaft system is mainly related to the fractal dimension  $D$ , the characteristic length scale  $G$ , the correction coefficient  $\chi$ , the elastic modulus  $E_1$ , the Poisson's ratio  $\nu_1$ , the yield strength  $Y$ , the actual maximum contact area  $a_{real}$  of asperities, the actual critical contact area  $a_{real}^c$ , the shaft angular position  $\theta$  and the articulation angle  $\delta$ . In engineering practice, more attention is paid to the fractal parameters (namely, the fractal dimension and the characteristic length scale), the material parameters (namely, the elastic modulus, the Poisson's ratio and the yield strength), the operating conditions (namely, the articulation angle and the shaft angular position) and the correction coefficient, because these parameters are designable parameters of the drive-shaft system. Thus, the fractal parameters, the material parameters and the correction coefficient are taken as the influencing factors of the NGAF in this paper. It should be noted that the actual maximum contact area  $a_{real}$  can be determined by combining Eqs. (6) and (45) under a certain input torque, as well the actual critical contact area  $a_{real}^c$  can be calculated by Eqs. (20) and (44).

Different from Eq. (13), Equation (49) contains the fractal parameters, the material parameters and the correction coefficient, which are related to the micro contact and friction characteristics between rollers and tracks. Equation (49), thus, can be used to study the deeper causes of the NGAF of the drive-shaft system, and it can provide an important reference for the design and development of the drive-shaft system.

## 4. Experiments and numerical analysis examples

### 4.1 Identification of the fractal dimension and the characteristic length scale

The fractal dimension  $D$  and the characteristic length scale  $G$  are important parameters of the fractal model of the NGAF. Before the validation of the fractal model of the NGAF, the fractal dimension  $D$  and the characteristic length scale  $G$  need to be identified. In general, the fractal dimension and the characteristic length scale can be identified by combining the measured rough surface profile and the structure-function method [27-29]. However, this identification process is complicated. In order to identify the fractal

parameters between the roller and the track more effectively, this paper first identifies the fractal dimension through the approximate relationship between the fractal dimension and the roughness, and then identifies the characteristic length scale through minimization of errors between the measured friction coefficient and the friction coefficient calculated by the fractal model of the friction coefficient (Eq. (48)).

According to the literature [30], the fractal dimension  $D$  of the rough surface can be approximated by the following formula:

$$D = \frac{1.528}{R_a^{0.042}} \quad (50)$$

where  $R_a$  is the roughness value of a rough surface.

Taking a drive-shaft system as the research object, the surface roughness  $R_a$  of the track inside the tripod joints is  $0.8\mu\text{m}$ . According to Eq. (50), the value of the fractal dimension  $D$ , thus, can be calculated as 1.54. For the characteristic length scale  $G$ , it is identified through minimization of errors between the friction coefficient calculated by the fractal model of the friction coefficient (Eq. (48)) and the measured friction coefficient. For the studied drive-shaft system in this paper, the measured friction coefficient between the roller and the track is 0.31, and other related parameters of the drive-shaft system are shown in Table 2, which are provided by the manufacturer [25]. Thus, when  $\mu=0.31$ ,  $D=1.54$  and other input parameters of the fractal model are shown in Table 2, the characteristic length scale  $G$  can be identified as  $5.1\times10^{-10}\text{m}$ .

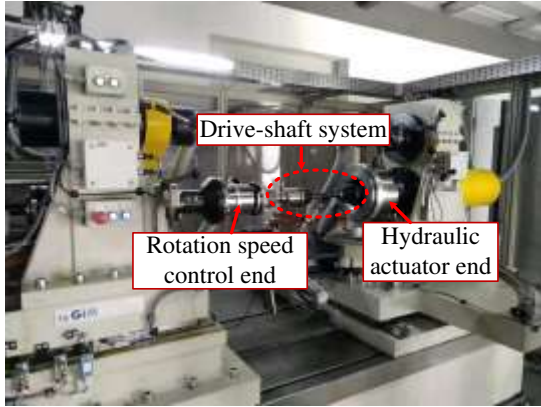
Table 2: Related parameters of the drive-shaft system [25].

Parameters	Unit	Value	Parameters	Unit	Value
PCR $r$ of the tripod joint	mm	30	Input torque $T$	Nm	100
Radius $R_2$ of the roller	mm	18.2	Elastic modulus $E_1$	GPa	210
Radius $R_1$ of the track cross section	mm	18.3	Poisson's ratio $\nu_1$	/	0.3
Arc angle $\alpha$ of the track cross section	°	270	Yield strength $Y$	MPa	320
Length $L_t$ of the track	mm	60			

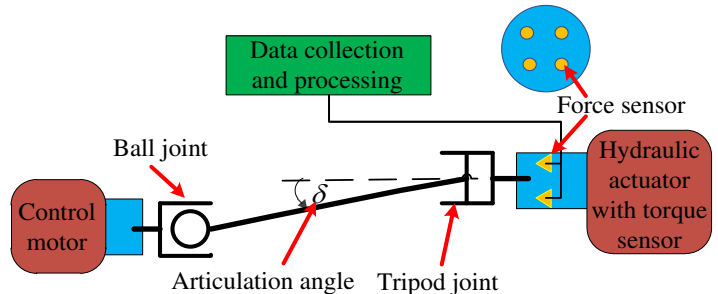
## 4.2 Measurements and model verification

To validate the fractal model of the NGAF of the drive-shaft system, a test bench is designed for measuring the NGAF of the drive-shaft system. The pictorial illustration and the schematic diagram of the test bench are shown in Figs. 8(a) and 8(b), respectively. The detailed measurement method for the NGAF of a drive-shaft system have been introduced in [31]. In brief, the ball joint is connected to a control motor, while the tripod joint is connected to a hydraulic actuator, as shown in Fig. 8(b). During the measurement, the hydraulic actuator applies an input torque, while the control motor applies a rotation speed. By adjusting the relative position of the hydraulic actuator end and the control motor end, a specified articulation angle can be determined. At the hydraulic actuator end, four force sensors are evenly installed to measure the

NGAF of the drive-shaft system, as shown in Fig. 8(b).



(a)



(b)

Fig. 8: (a) Pictorial illustration; and (b) schematic diagram of the test bench of the drive-shaft system.

Taking a drive-shaft system as the test object, the dimension parameters, the material parameters and the input torque of the drive-shaft system are shown in Table 2. Through the identification in Section 4.1, the fractal dimension and the characteristic length scale are obtained as 1.54 and  $5.1 \times 10^{-10}$ m, respectively. Substituting the parameters shown in Table 2 and the identified fractal dimension and characteristic length scale into Eq. (49), the NGAF of the drive-shaft system at different articulation angles ( $0^\circ$ - $16^\circ$ ) can be determined, as shown in Fig. 9. Meanwhile, the measured NGAF at different articulation angles ( $0^\circ$ - $16^\circ$ ) can be obtained on the basis of the test bench of the drive-shaft system, and the measured results are also shown in Fig. 9. During the measurement, the input torque is set as 100Nm, as well the rotation speed is set as 200rpm [25]. In addition, since the influence of grease is not considered in the proposed fractal model of the NGAF of the drive-shaft system, the grease inside the tripod joint is cleaned. It is seen from Fig. 9 that the calculated NGAF is basically consistent with the measured NGAF, indicating the effectiveness of the NGAF fractal model of the drive-shaft system.

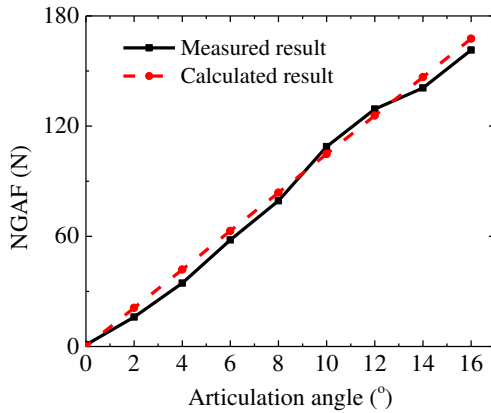


Fig. 9: Comparisons of the NGAF calculated by the fractal model and the NGAF measured by the test bench at different articulation angles.

#### 4.3 Effects of factors on the NGAF

According to the analysis in Section 3.5, the main factors influencing the NGAF include the fractal

parameters (namely, the fractal dimension and the characteristic length scale), the material parameters (namely, the elastic modulus, the Poisson's ratio and the yield strength), the operating conditions (namely, the articulation angle and the shaft angular position) and the correction coefficient. Since the effects of the operating conditions on the NGAF have been analyzed in [18,31], this section only analyzes the effects of the fractal parameters, the material parameters and the correction coefficient on the NGAF. The initial analysis values of the input parameters of the NGAF fractal model (Eq. (49)) are shown in Table 3.

In Table 3, the size parameters and material parameters related to the tripod joint are the design parameters of an existing tripod joint, which are supplied by the manufacturer [25]; the initial analysis value of the input torque remains consistent with the test condition in Section 4.2; and  $6^\circ$  is the design value of the articulation angle of the drive-shaft system [25]. According to the analysis in Section 2.3, the magnitude of the AFF reaches the maximum when the shaft angular position is  $90^\circ$ , and thus the initial analysis value of the shaft angular position is set as  $90^\circ$ . In addition, the correction coefficient is calculated by substituting the size parameters and material parameters related to the tripod joint as well as the input torque into Eq. (41), as well the fractal dimension and the characteristic length scale are obtained by identifying the rough surface characteristics between the rollers and tracks inside the tripod joint, as described in Section 4.1.

It should be pointed out that the correction coefficient, the fractal dimension and the characteristic length scale are important parameters that characterize the real rough surface characteristics between the roller and the track. The correction coefficient corrects the contact shape and contact state between the roller and the track by modifying the distribution of asperities between the roller and the track, as well the fractal dimension and the characteristic length scale directly reflect the roughness and the rough surface profiles between the roller and the track.

Table 3: Initial analysis values of the input parameters of the fractal model.

Input parameters	Unit	Value	Input parameters	Unit	Value
PCR $r$ of the tripod joint	mm	30	Poisson's ratios $\nu_1$	/	0.3
Radius $R_2$ of the roller	mm	18.2	Input torque $T$	Nm	100
Length $L_t$ of the track	mm	60	Articulation angle $\delta$	$^\circ$	6
Radius $R_1$ of the track cross section	mm	18.3	Shaft angular position $\theta$	$^\circ$	90
Arc angle $\alpha$ of the track cross section	$^\circ$	270	Collection coefficient $\chi$	/	0.666
Yield strength $Y$	MPa	320	Fractal dimension $D$	/	1.54
Elastic modulus $E_1$	GPa	210	Characteristic length scale $G$	m	$5.1 \times 10^{-10}$

### (1) Effects of the fractal dimension and the characteristic length scale on the NGAF

When magnitudes of the characteristic length scale are  $1 \times 10^{-10}$ m,  $5 \times 10^{-10}$ m and  $10 \times 10^{-10}$ m, respectively, and other parameters are shown in Table 3, the relationship between the NGAF and the fractal dimension is shown in Fig. 10(a). It is seen that with the increase of the fractal dimension, the NGAF first

increases and then decreases. When the fractal dimension is about 1.63, the NGAF reaches the maximum value. According to the analysis in [10], with the increase of the fractal dimension  $D$ , the critical contact area decreases, and then a large number of asperities in the elastic stage increase; when the fractal dimension increases to a specific value, the asperities in the elastic stage increases to the limit; as the fractal dimension continues to increase, the percentage of asperities in the elastic stage decreases since a large number of asperities smaller than the critical contact area increase.

Thus, when the fractal dimension is in the range of [1.45,1.63], with the increase of the fractal dimension, the tangential contact force between the roller and the track increases due to the increase of asperities in the elastic stage, which leads to the increase of the NGAF. When the fractal dimension is in the range of [1.63, 1.95], with the increase of the fractal dimension, the tangential contact force between the roller and the track decreases due to the decrease of the percentage of asperities in the elastic stage, which leads to the decrease of the NGAF. In addition, when the fractal dimension is greater than 1.63, according to Eq. (50), the smaller the fractal dimension is, the rougher the contact surface will be. In this case, the NGAF of a drive-shaft system can be reduced by improving the machining precision of contact surfaces between the roller and the track.

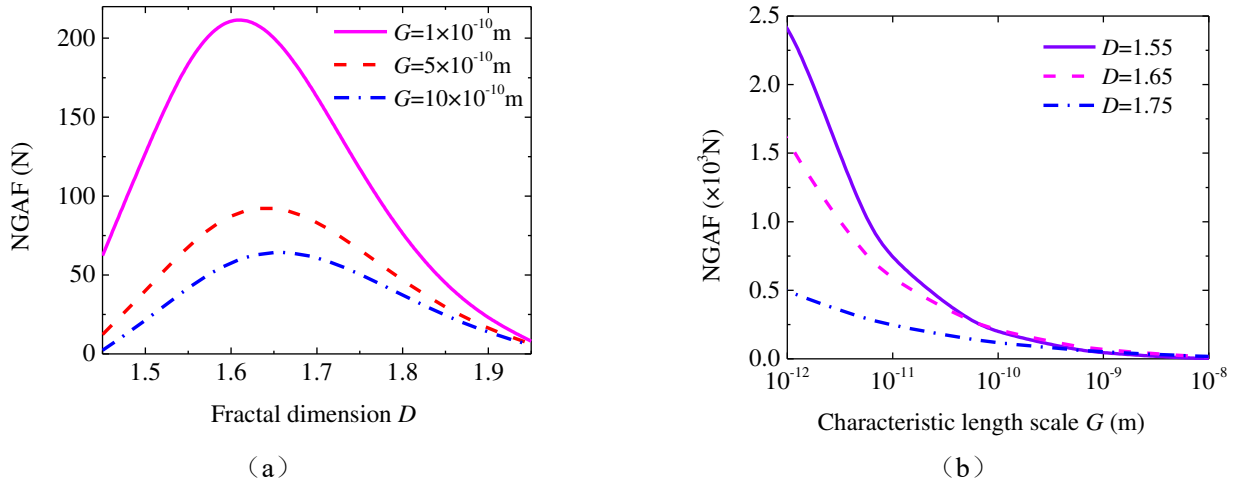


Fig. 10: Variations in the NGAF with (a) the fractal dimension; and (b) the characteristic length scale.

When fractal dimensions are 1.55, 1.65, and 1.75, respectively, and other parameters are shown in Table 3, the relationship between the NGAF and the characteristic length scale is shown in Fig. 10(b). It is seen that with the increase of the characteristic length scale, the NGAF decreases. This is because with the increase of the characteristic length scale, the radius of asperities decreases and the percentage of asperities in the elastic stage decreases [10], and thus the tangential contact force between the roller and the track will decreases. The NGAF thus can be reduced by reducing the characteristic length scale that affects the profile of the rough surface.

## (2) Effects of the yield strength, the Poisson's ratio and the elastic modulus on the NGAF

Figures 11(a), 11(b) and 11(c) illustrate variations in the NGAF with variations in the yield strength, the Poisson's ratio and the elastic modulus, respectively. The results presented for two different fractal dimensions (1.55 and 1.65) suggest that the NGAF increases with the increase of the yield strength and the Poisson's ratio, while the NGAF decreases with the increase of the elastic modulus. This is because under a certain load, with the decrease of the elastic modulus and the increase of the yield strength and the Poisson's ratio, more asperities in the plastic deformation stage turn to the elastic deformation stage, which leads to the increase of the percentage of the asperities in the elastic deformation stage. Therefore, by increasing the elastic modulus and reducing the yield strength and the Poisson's ratio, the NGAF can be reduced effectively.

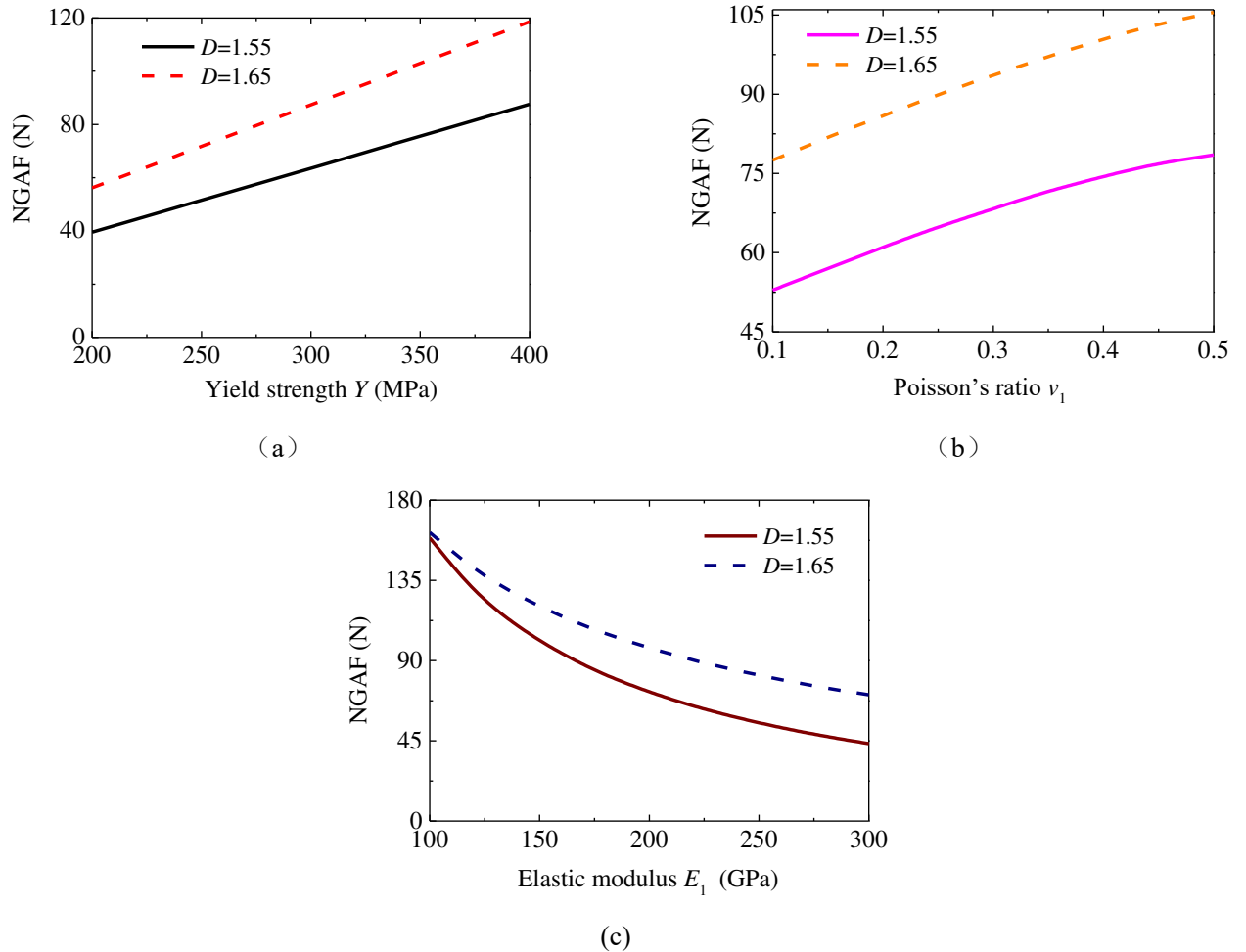


Fig. 11: Variations in the NGAF with (a) the yield strength; (b) the Poisson's ratio; and (c) the elastic modulus.

### (3) Effects of the correction coefficient on the NGAF

Figure 12 illustrates the variation in the NGAF with the variation in the correction coefficient for two different fractal dimensions (1.55 and 1.65). The results suggest that the NGAF decreases with the increase of the correction coefficient. Under a certain load, when the correction coefficient increases, it means that the contact area between the roller and the track increases, which lead to an increase in the number of asperities and then a decrease in the load borne by each asperity. If the load borne by each asperity decreases,

its contact area is likely to be smaller than the critical contact area, and thus more asperities are in the plastic deformation stage. Thus, with the increase of the correction coefficient, the tangential contact force between the roller and the track decreases, resulting in the decrease of the NGAF.

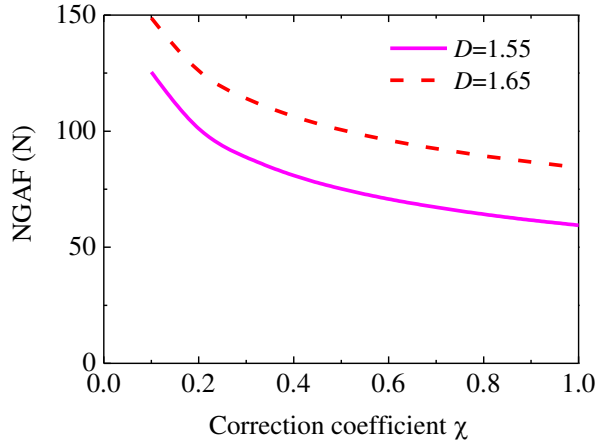


Fig. 12: Variation in the NGAF with the correction coefficient.

In summary, in addition to the yield strength, other influencing factors, namely, the fractal parameters, the Poisson's ratio, the elastic modulus and the correction coefficient, all have a nonlinear effect on the NGAF. Moreover, the influencing factors (including the fractal parameters, the material parameters and the correction coefficient) affect the magnitude of the NGAF by affecting the percentage of contact asperities between the roller and the track in the elastic stage. According to the above analyses, it is seen that the relationships between the NGAF and the influencing factors can be studied and revealed from the micro level on the basis of the proposed fractal model of the NGAF, which will provide an important reference for reducing the NGAF and the design of the drive-shaft system.

#### 4.4 Sensitivity analysis of the fractal model of the NGAF

To further determine effects of the factors in Section 4.3 on the NGAF, the sensitivity analysis of the fractal model (Eq. (49)) of the NGAF is carried out by using Sobol' global sensitivity method [32]. The main ideal of Sobol' global sensitivity method is to decompose the model into the sum of  $2^n$  incremental terms, and then calculate the deviation and total variance of the model response through sampling, so as to obtain the first order global sensitivity and the overall global sensitivity of the model. In the sensitivity analysis, the value ranges of the fractal dimension, the characteristic length scale, the elastic modulus, the Poisson's ratio, the yield strength, the articulation angle, the shaft angular position and the correction coefficient are shown in Table 4, as well other input parameters of the fractal model (Eq. (49)) are shown in Table 3.

When 1,000,000 random samples are sampled for the influencing factors in Table 4, the sensitivity analysis results are shown in Table 5. It is seen that comparing with the fractal dimension, the shaft angular

position, the Poisson's ratio, the yield strength and the correction coefficient, the first order global sensitivity coefficients of the characteristic length scale, the elastic modulus and the articulation angle are larger, and thus these factors have a greater influence on the NGAF. In addition, for the characteristic length scale, the elastic modulus and the articulation angle, the absolute differences between their first order global sensitivity coefficients and their overall global sensitivity coefficients are large, which indicates that there is a large interaction among these influencing factors on the NGAF. According to the overall global sensitivity, influences of the considered factors on the NGAF are ranked from top to bottom as follows: the articulation angle, the characteristic length scale, the elastic modulus, the yield strength, the fractal dimension, the shaft angular position, the Poisson's ratio and the correction coefficient.

Table 4: Value ranges of the factors influencing the NGAF.

Parameter	Definition	Unit	Value range
$D$	Fractal dimension	/	[1.5, 1.7]
$G$	Characteristic length scale	$\times 10^{-10} \text{m}$	[1, 10]
$Y$	Yield strength	MPa	[200, 400]
$E_1$	Elastic modulus	GPa	[100, 300]
$\nu_1$	Poisson's ratio	/	[0.1, 0.5]
$\theta$	Shaft angular position	°	[60, 120]
$\delta$	Articulation angle	°	[2, 10]
$\chi$	Correction coefficient	/	[0.5, 1]

Table 5: First order and overall global sensitivities of the fractal model of the NGAF.

Factor	First order global sensitivity (%)	Overall global sensitivity (%)	Absolute value of differences (%)
Fractal dimension $D$	4.08	5.82	1.74
Characteristic length scale $G$	21.36	27.17	5.81
Elastic modulus $E_1$	39.19	19.24	19.95
Yield strength $Y$	6.76	9.54	2.78
Poisson's ratio $\nu_1$	1.23	1.58	0.35
Articulation angle $\delta$	23.45	30.52	7.07
Shaft angular position $\theta$	3.53	5.39	1.86
Correction coefficient $\chi$	0.40	0.75	0.34

## 5. Conclusion

The method for correcting the distribution of asperities between the roller and the track as well as the fractal model of the NGAF proposed in this paper are effective and useful for revealing the relationships between the NGAF and the influencing factors (including the fractal parameters, the material parameters and the correction coefficient) from the micro level, which will provide an important reference for reducing the NGAF and the design of the drive-shaft system.

The influencing factors affect the magnitude of the NGAF strongly by affecting the percentage of

contact asperities between the roller and the track in the elastic stage. With the increase of the fractal dimension, the NGAF first increases and then decreases. By improving the machining precision of contact surfaces between the roller and the track, the NGAF of a drive-shaft system can be reduced when the fractal dimension is large. The results suggest decrease in the NGAF with increasing the characteristic length scale, and thus the NGAF can be reduced by reducing the characteristic length scale. The NGAF increases with the increase of the yield strength, while the NGAF decreases with the increase of the Poisson's ratio and the elastic modulus. Thus, the NGAF also can be reduced effectively by reducing the yield strength and increasing the Poisson's ratio and the elastic modulus. By changing the material and size parameters of the roller and the track, the correction coefficient can be increased, and then the NGAF can be reduced.

The Sobol' global sensitivity analysis quantitatively yields the influences of all the factors considered on the NGAF. According to the overall global sensitivity, influences of the considered factors on the NGAF are ranked from top to bottom as follows: the articulation angle, the characteristic length scale, the elastic modulus, the yield strength, the fractal dimension, the shaft angular position, the Poisson's ratio and the correction coefficient. Meanwhile, compared with other factors, there is a large interaction among the characteristic length scale, the elastic modulus and the articulation angle on the NGAF.

## Replication of results

The results of the above numerical analysis can be obtained through the Matlab code. The relevant Matlab code can be seen in the supplementary material.

## Acknowledgments

The authors acknowledge the Natural Science Foundation of Guangdong Province (Grant No. 2019A1515011612), and the National Natural Science Foundation of China (Grant No.11472107).

## Conflict of interest

The authors declare that they have no conflict of interest.

## References

- [1] C.H. Lee, A.A. Polycarpou (2006) Experimental investigation of tripod constant velocity (CV) joint friction, SAE Technical Paper no. 2006-01-0582.
- [2] C.H. Lee, A.A. Polycarpou (2010) A phenomenological friction model of tripod constant velocity (CV) joints. *Tribology International*, 43(4):844-858.
- [3] K H Lee, D W Lee, J H Chung, et al. (2014) Design of generated axial force measurement tester for tripod constant velocity joints under shudder condition. *Journal of Mechanical Science & Technology*, 28(10):4005-4010.
- [4] J S Sa, T W Kang, C M Kim (2010) Experimental study of the characteristics of idle vibrations that result from

- axial forces and the spider positions of constant velocity joints. International Journal of Automotive Technology, 11(3):355-361.
- [5] S Serveto, J P Mariot, M Diaby (2008) Modelling and measuring the axial force generated by tripod joint of automotive drive-shaft. Multibody System Dynamics, 19(3):209-226.
  - [6] G H Jo, S H Kim, D W Kim, et al. (2018) Estimation of generated axial force considering rolling-sliding friction in tripod type constant velocity joint. Tribology Transactions, 1-48.
  - [7] Y H Lim, M E Song, W H Lee, et al. (2009) Multibody dynamics analysis of the drive-shaft coupling of the ball and tripod types of constant velocity joints. Multibody System Dynamics, 22(2):145-162.
  - [8] Q C Cai, K H Lee, W L Song, et al. (2012) Simplified dynamics model for axial force in tripod constant velocity joint. International Journal of Automotive Technology, 13(5):751-757.
  - [9] A Majumdar and C L Tien. (1990) Fractal characterization and simulation of rough surfaces. Wear, 136: 313-327.
  - [10] A Majumdar and B Bhushan. (1991) Fractal model of elastic-plastic contact between rough surfaces. Journal of Tribology-transactions of the ASME, 113(1):1-11.
  - [11] Q Chen, Y Wang, W Tian, et al. (2019) An improved nonlinear dynamic model of gear pair with tooth surface microscopic features. Nonlinear Dynamics, 96:1615–1634.
  - [12] Z Li, Z Peng. (2016) Nonlinear dynamic response of a multi-degree of freedom gear system dynamic model coupled with tooth surface characters: a case study on coal cutters. Nonlinear Dynamics, 84: 271–286.
  - [13] D A H Hanaor, Y Gan, I Einav. (2015) Contact mechanics of fractal surfaces by spline assisted discretization. International Journal of Solids and Structures, 59: 121–131.
  - [14] Y Yuan, Y Cheng, K Liu, L Gan. (2017) A revised Majumdar and Bushan model of elastoplastic contact between rough surfaces. Applied Surface Science, 425: 1138-1157.
  - [15] Y Zhao, H Wu, Z Liu, et al. (2018) A novel nonlinear contact stiffness model of concrete–steel joint based on the fractal contact theory. Nonlinear Dynamics, 94: 151–164.
  - [16] S Jiang, Y Zheng and H Zhu. (2010) A contact stiffness model of machined plane joint based on fractal theory. Journal of Tribology-transactions of the ASME, 132: 011401.
  - [17] Y Liu, B Shangguan, Z Xu. (2012) A friction contact stiffness model of fractal geometry in forced response analysis of a shrouded blade. Nonlinear Dynamics, 70: 2247–2257.
  - [18] H Y Feng, S Rakheja, W B Shangguan. (2020) Analysis and optimization for generated axial force of a drive-shaft system with interval uncertainty. Structural and Multidisciplinary Optimization, 63(1): 197-210.
  - [19] Y. Yuan, K. Xu, K. Zhao. (2020) The Loading–Unloading Model of Contact Between Fractal Rough Surfaces. International Journal of Precision Engineering and Manufacturing. <https://doi.org/10.1007/s12541-020-00330-y>.
  - [20] L Wei, Q Liu and P Zhang. (2012) Sliding friction surface contact mechanics model based on fractal theory. Chinese Journal of Mechanical Engineering, 48(17): 106-113.
  - [21] J Sun, Z Ji and C Ma. (2018) Research of the contact mechanics for rough surfaces. Chinese Journal of Theoretical and Applied Mechanics, 50(1): 68-77.
  - [22] J Liu, C Ma, S Wang, et al. (2019) Contact stiffness of spindle-tool holder based on fractal theory and multi-scale contact mechanics model. Mechanical Systems and Signal Processing, 119: 363-379.
  - [23] Q Chen, F Xu, P Liu and H Fan. (2016) Research on fractal model of normal contact stiffness between two spheroidal joint surfaces considering friction factor. Tribology International, 97: 253-264.

- [24] Johnson K L. Contact Mechanics. University of Cambridge, 1985.
- [25] Y Luo (2020) Personal communications. Zhejiang Xianglong Machinery Co., Ltd., Ningbo, China.
- [26] G Lan, X Zhang, H Ding, et al. (2012) Modified model of static friction coefficient of joint interfaces based on fractal theory. *Transactions of the Chinese Society for Agricultural Machinery*, 43(1): 213-218.
- [27] Z. Liu, T. Zhang, Y. Wang, C. Yang, et al. (2019) Experimental Studies on Torsional Stiffness of Cycloid Gear Based on Machining Parameters of Tooth Surfaces. *International Journal of Precision Engineering and Manufacturing*, 20:1017–1025.
- [28] Y. Liu, Q. Meng, X. Yan, S. Zhao, et al. (2019) Research on the solution method for thermal contact conductance between circular-arc contact surfaces based on fractal theory. *International Journal of Heat and Mass Transfer*, 145: 118740.
- [29] P. Xue, C. Zhu, R. Wang and L. Zhu. (2020) Research on dynamic characteristics of oil-bearing joint surface in slide guides. *Mechanics Based Design of Structures and Machines*, <https://doi.org/10.1080/15397734.2020.1766493>.
- [30] P Liu, H Zhao, K Huang, et al. (2018) Research on normal contact stiffness of micro-segments gear based on improved fractal model. *Chinese Journal of Mechanical Engineering*, 54(7): 114-122.
- [31] H Feng, S Rakheja, W B Shangguan (2020) Analytical and experimental analysis of axial force generated by a drive-shaft system. *Proceedings of the IMechE, Part K: Journal of Multi-body Dynamics*, 0(0):1-16.
- [32] I M Sobol'. (2001) Global sensitivity indices for nonlinear mathematical models and their Monte Carlo estimates. *Mathematics and Computers in Simulation*, 55(1-3):271-280.

## Figures

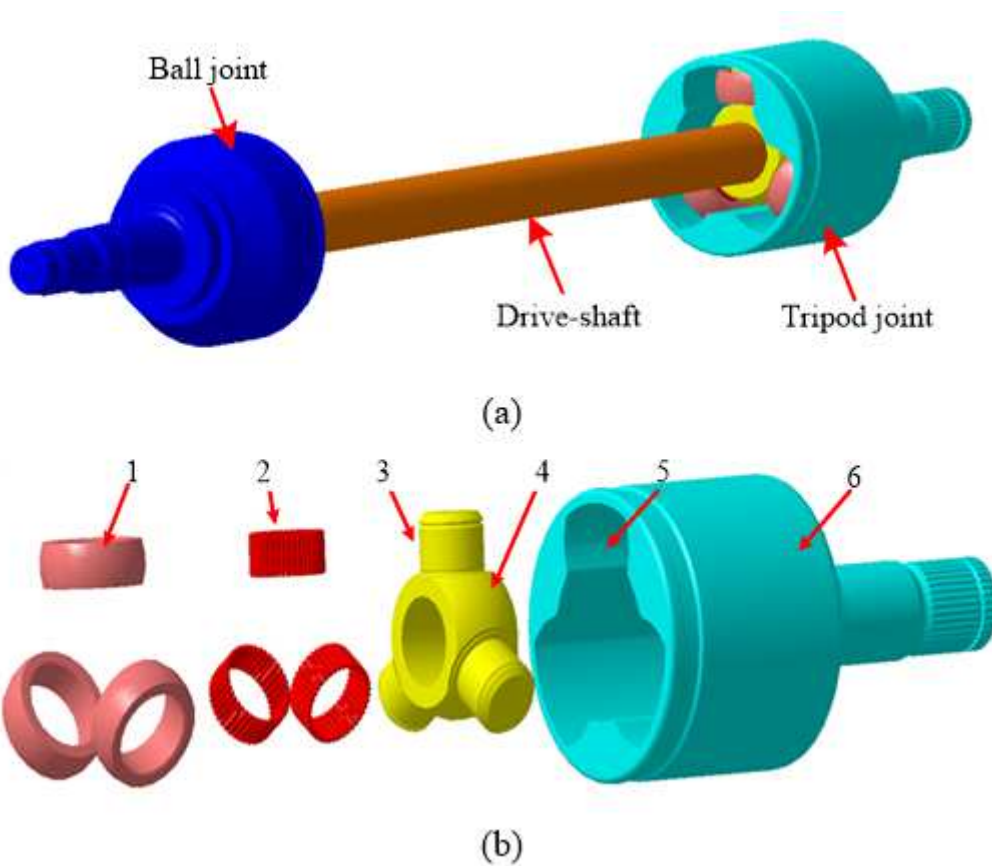


Figure 1

(a) Structure of a drive-shaft system; and (b) Structure of a tripod joint. (1-roller; 2-needle; 3-trunnion; 4-tripod; 5-track; 6-housing)

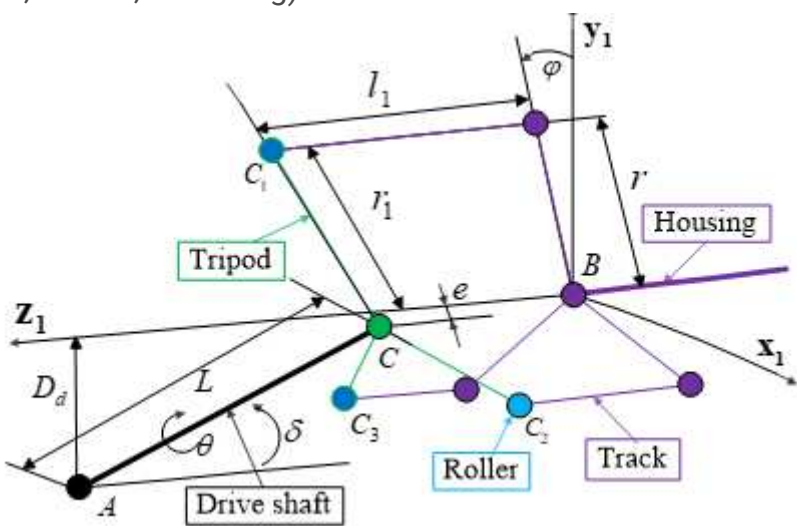
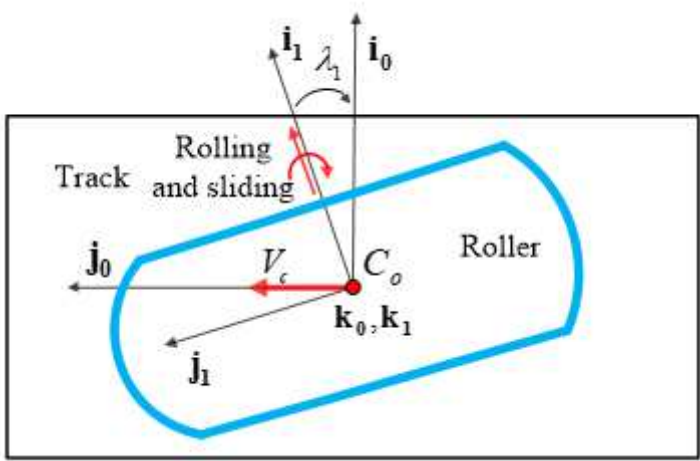


Figure 2

Schematic diagram of the kinematic model of a drive-shaft system.



**Figure 3**

Schematic diagram of the motion of roller C1 on the tracks.

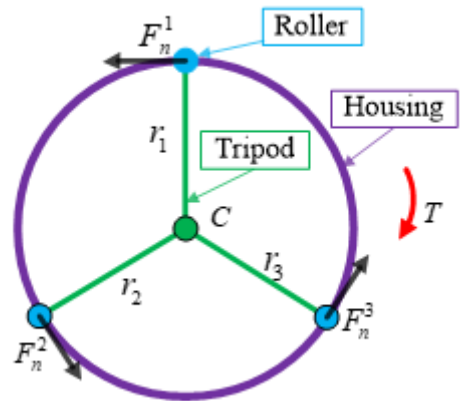


**Figure 4**

Schematic diagram of the normal force of rollers acting on tracks.

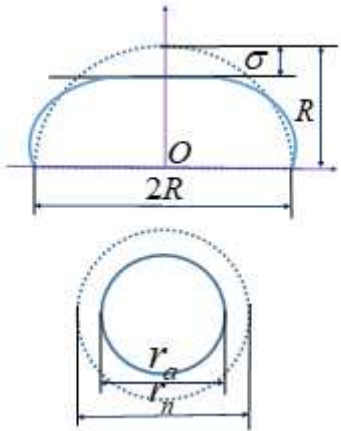


**Figure 5**

Schematic diagram of the deformation of a contact spot.

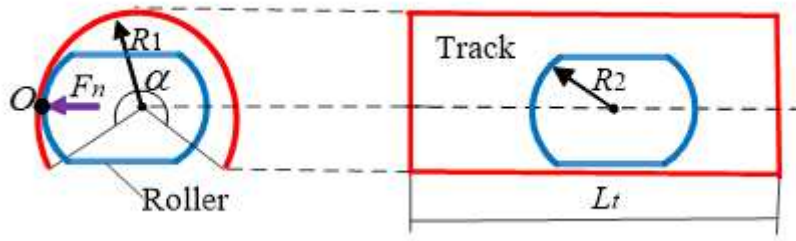


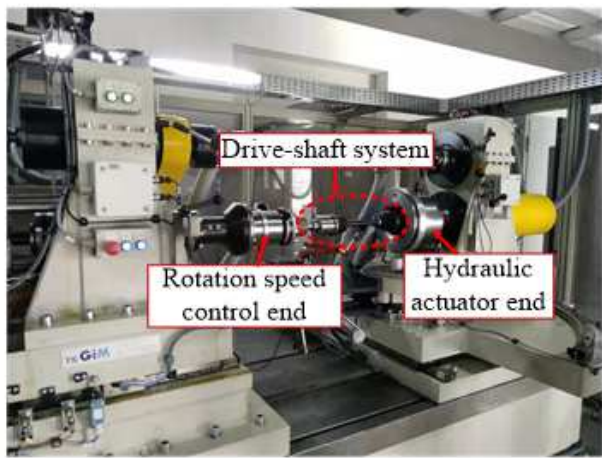
**Figure 6**

Schematic diagram of the contact between the roller and the track.

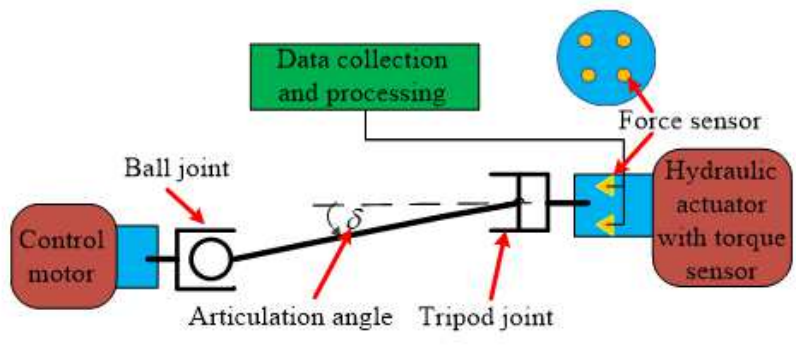


**Figure 7**

(a) Schematic diagram of the static contact between two curved surfaces; and (b) schematic diagram of the coordinates of the two surfaces at the contact point O.



(a)



(b)

**Figure 8**

(a) Pictorial illustration; and (b) schematic diagram of the test bench of the drive-shaft system.

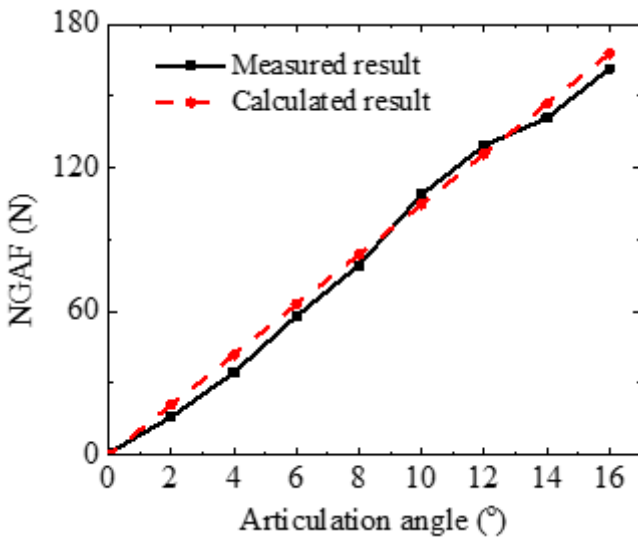
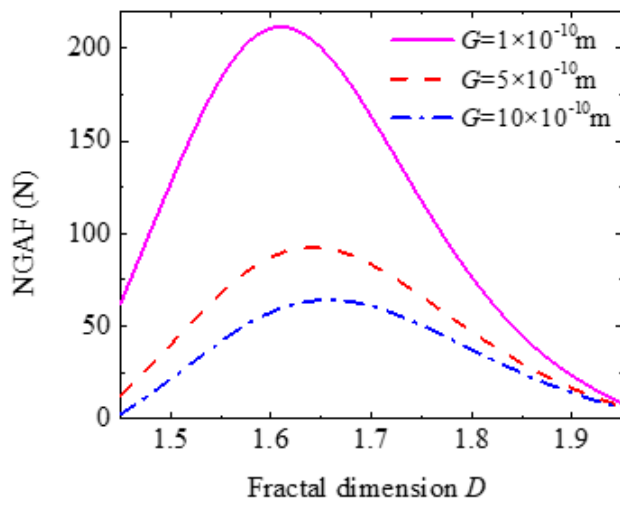
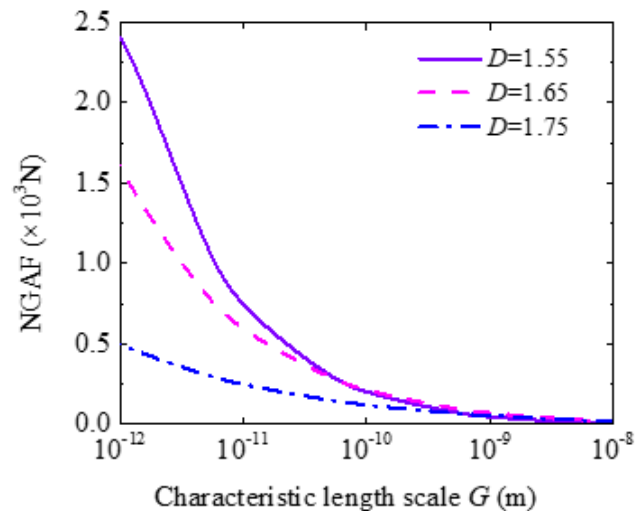


**Figure 9**

Comparisons of the NGAF calculated by the fractal model and the NGAF measured by the test bench at different articulation angles.



(a)



(b)

**Figure 10**

Variations in the NGAF with (a) the fractal dimension; and (b) the characteristic length scale.

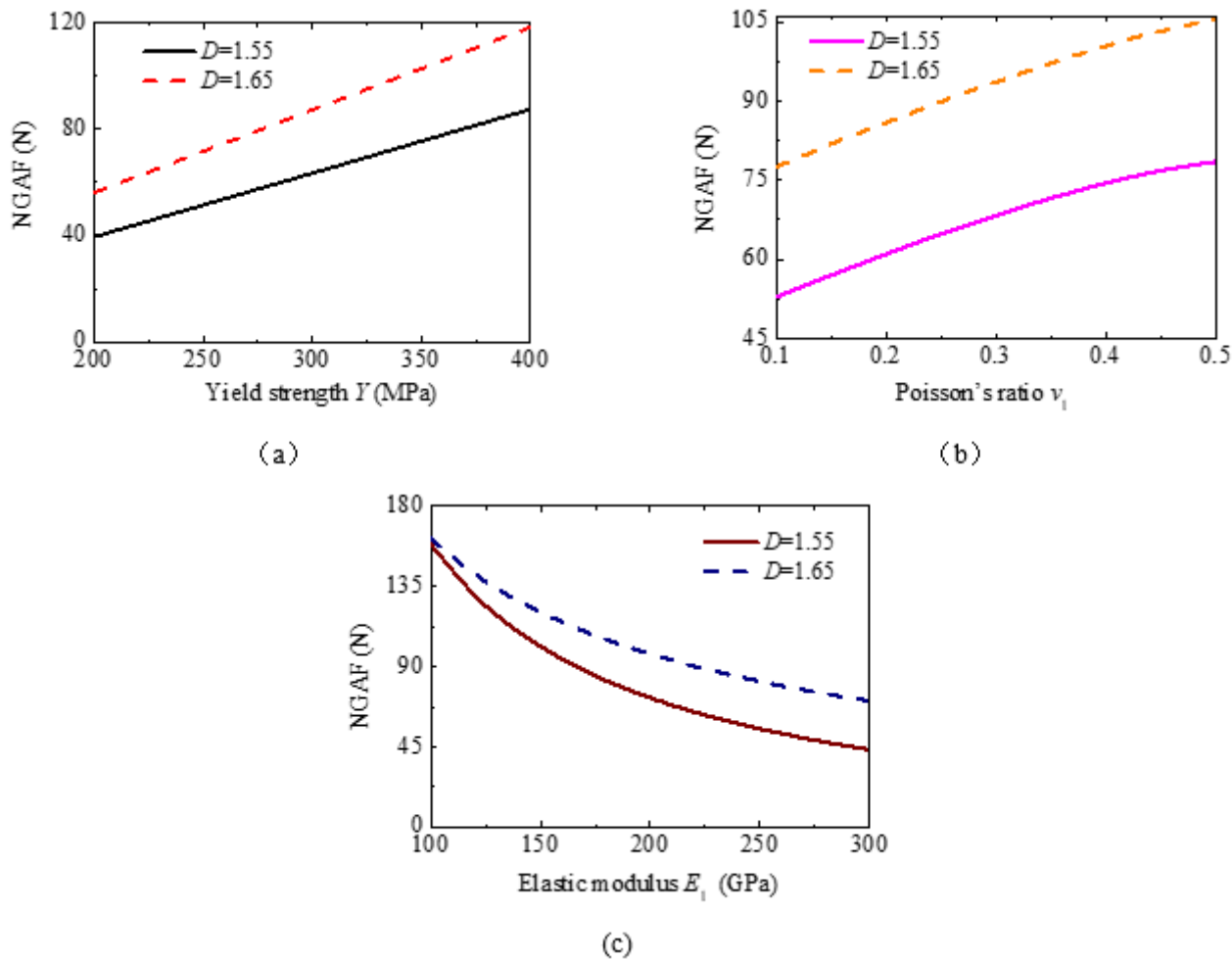


**Figure 11**

Variations in the NGAF with (a) the yield strength; (b) the Poisson's ratio; and (c) the elastic modulus.

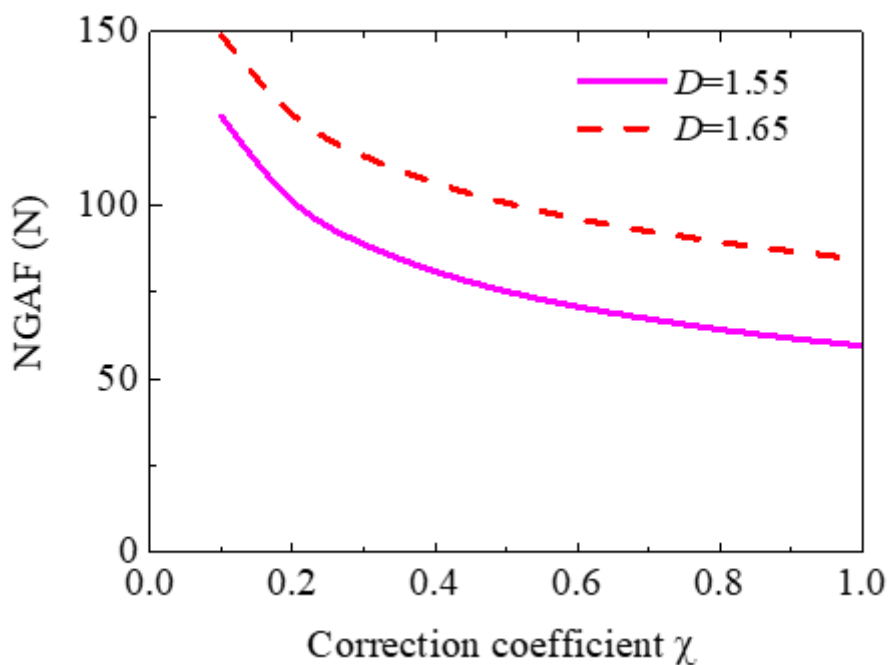


## **Figure 12**

Variation in the NGAF with the correction coefficient.